Effect of exchange and dipolar interlayer interactions on the magnonic band structure of dense Fe/Cu/Py nanowires with symmetric and asymmetric layer widths

G. Gubbiotti [1,*] X. Zhou,[2] A. O. Adeyeye [2,†] G. Varvaro [3] and M. Kostylev [4]

[1]*Istituto Officina dei Materiali del CNR (CNR-IOM), Sede Secondaria di Perugia, c/o Dipartimento di Fisica e Geologia, Università di Perugia, I-06123 Perugia, Italy*

[2]*Information Storage Materials Laboratory, Department of Electrical and Computer Engineering, National University of Singapore, 117576 Singapore*

[3]*Istituto di Struttura della Materia – CNR, nM^2-Lab, Area della Ricerca Roma 1, Via Salaria km 29.300, 00015 Monterotondo Scalo (Roma) - Italy*

[4]*Department of Physics and Astrophysics, University of Western Australia, 35 Stirling Hwy, 6009 Western Australia, Australia*

(Received 10 October 2019; revised manuscript received 10 January 2020; accepted 1 June 2020; published 24 June 2020)

We present a systematic experimental and theoretical investigation of the magnonic band structure in dense arrays of both asymmetric and symmetric cross-section trilayered Fe(10 nm)/Cu(t)/Py(10 nm) nanowires (NWs). The Cu spacer thickness (t) is varied in the range between 0 and 10 nm. The frequency dispersion of collective spin-wave excitations in the above trilayered NW arrays has been studied by the Brillouin light-scattering technique while sweeping the wave vector perpendicularly to the nanowire length over four Brillouin zones of the reciprocal space. The experimental results have been quantitatively reproduced by an original numerical model that includes a two-dimensional Green's function description of the dipole field of the dynamic magnetization and exchange coupling between the layers. We found that, depending on t, the Py and Fe magnetic layers within the same nanowire are coupled by either the interlayer exchange or dipolar interactions. This has an impact on both the magnetization reversal and the collective dynamical properties of the artificial crystal. In particular, it is possible to stabilize a magnetization configuration where the layer magnetization vectors point in the same or in the opposite direction over a field range that varies with the Cu thickness. In addition, several modes are detected whose propagation properties (i.e., stationary or dispersive) through the array depend on static magnetization configuration as well as on the relative phase (in-phase or out-of-phase) of dynamic magnetizations between the two layers within the same nanowire.

DOI: 10.1103/PhysRevB.101.224431

I. INTRODUCTION

Magnonic crystals (MCs) are metamaterials with periodical spatial variation of their magnetic properties and exhibit novel features such as the formation of magnonic band gaps that do not exist in natural magnetic structures [1]. MCs offer novel possibility to tune their band structure in a reconfigurable manner [2–5] in order to control and manipulate spin waves (SWs) in magnonic devices such as transistors, filters, sensors, and logic gates [6–9]. The use of SWs for carrying and processing information is very promising for building ultralow power-consuming magnetic devices which employ the magnon current rather than the charge current.

The magnonic band structure of long-wavelength SWs in one-dimensional bicomponent magnonic crystals (BMCs) in the form of a periodic array of alternating contacting Permalloy (Py) and cobalt magnetic nanowires (NWs) have been widely investigated by Brillouin light-scattering (BLS) spectroscopy from thermally excited SWs [10–12]. The observed band gaps were found to be tunable by varying the lattice constant as well as the applied magnetic-field strength. In two dimensions (2D), BMCs in the form of antidot lattices with holes filled by another ferromagnetic material have widely been investigated in detail and used as a model system to investigate the SW propagation in nanochannels [13,14] and the dependence of the magnonic band-gap width on both the filling fraction and the magnetic contrast of the constituent materials [15,16]. Remarkably, most of the BMCs investigated up to now are planar nanostructures with homogeneous thickness of the different components [17,18] while investigation of three-dimensional crystals are essentially limited to theoretical studies [19,20].

In this work, we present a combined experimental and theoretical study of the magnonic band structure of arrays of closely spaced trilayered Fe(10 nm)/Cu(t)/Py(10 nm) NWs with either symmetric (rectangular) and asymmetric (L-shaped) shapes of NW cross section as a function of the thickness of the Cu spacer (t) that is varied in the range from 0 to 10 nm. With respect to the previous studies on

*gubbiotti@iom.cnr.it

†Present Address: Department of Physics, Durham University, South Rd, Durham DH1 3LE, United Kingdom.

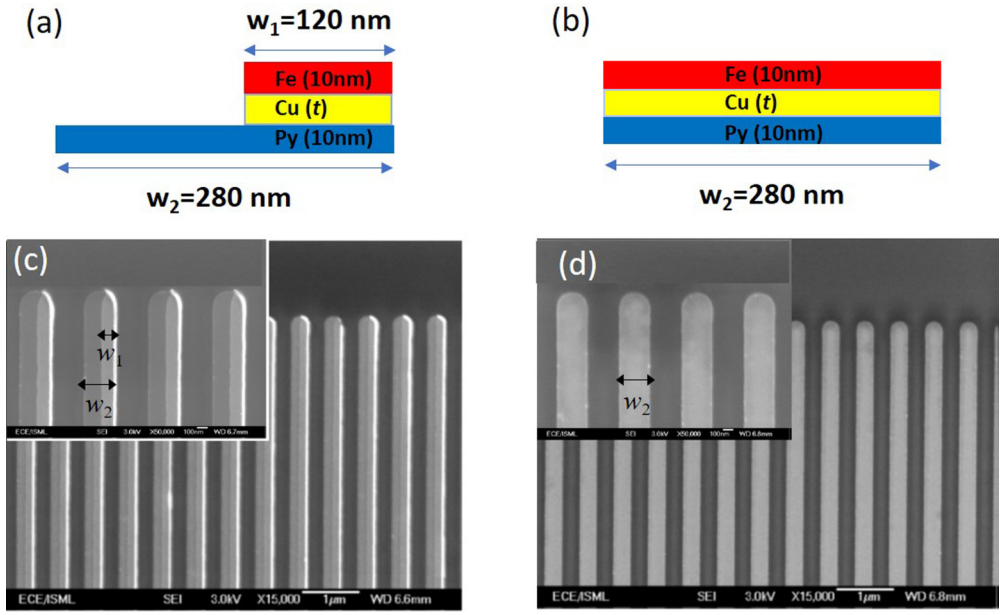

FIG. 1. Sketch of the geometry and layering sequence of the investigated L-shaped (a) and rectangular (b) NWs together with SEM images (top view) of the NWs L-shaped (c) and rectangular (d) cross section for $t = 2.5$ nm. Width of the top (w_1) and bottom (w_2) layers are indicated by the arrows in the zoomed region.

Fe/Py NW arrays [21,22], the present paper shows that, depending on the Cu thickness, the magnetization reversal of the Py and Fe NW layers can be coupled by either the interlayer exchange and dipolar interactions, or by the dipolar interaction alone. This offers unique opportunities for understanding the interplay between static and dynamic interactions acting within any NW and between adjacent NWs [23,24]. The dispersion of collective SWs has been measured by wave-vector-resolved BLS spectroscopy. This technique has proven to be a very powerful tool for studying the magnetization dynamics in magnetic thin and ultrathin films [25,26], multilayers [27], and patterned structures [28–31], since it combines the possibility to measure SWs in a wide frequency range (1–100 GHz) with wave vectors continuously selectable up to $10^7 \mathrm{m}^{-1}$ and with an extremely high sensitivity.

The knowledge of the magnonic band structure is an important prerequisite for successful design of microwave devices based on spin waves. Periodic arrays of magnetic nanowires are prospective candidates for electrically tunable microwave bandpass and band-stop filters based on traveling spin waves. In the case of the layered nanowires, the passband/stop-band frequency width and central frequency depend on the interlayer interaction (i.e., exchange or dipolar) between the ferromagnetic layers. Accordingly, the layered nanowire arrays have an important advantage over those based on single-layer magnetic materials. This is an extra channel for controlling central frequencies of the bands. This channel is the static magnetization configuration for the wires that depends on the magnetic history of the wire array.

Here we explain the physical mechanisms underlying formation of the propagative and stationary modes. These layered nanowires represent a step forward towards implementation of vertically integrated three-dimensional field-reconfigurable magnonic devices [32–36].

II. SAMPLE FABRICATION AND MEASUREMENTS

Large-area ($4 \times 4\,\mathrm{mm}^2$) trilayered $[\mathrm{Fe/Cu}(t)]_{(w1)}/\mathrm{Py}_{(w2)}$ NW arrays were fabricated using a combination of the deep ultraviolet lithography resist template at 248-nm exposure wavelength and the self-aligned shadow-deposition method [32]. NW arrays containing four different values of the Cu spacer thickness ($t = 0$, 2.5, 5.0, and 10 nm) were prepared while the Py ($\mathrm{Ni_{80}Fe_{20}}$) and Fe thicknesses are fixed at 10 nm. For the L-shaped NWs, the width of the top Fe/Cu NW layers is $w_1 = 120$ nm while the Py layer is $w_2 = 280$ nm wide. For the rectangular cross-section NWs, all the NW layers have the same width, $w_1 = w_2 = 280$ nm. The NW length is 4 mm, the edge to edge separation is $s = 280$ nm (as measured at the level of the bottom layer) while the array periodicity is $a = (w_1 + s) = 560$ nm, resulting in the edge of the first Brillouin-zone (BZ) value $\pi/a = 0.56 \times 10^7 \mathrm{rad/m}$. The scanning electron microscope (SEM) images of the L-shaped and rectangular cross-section Fe/Cu/Py Nws with Cu spacer thiciness of $t = 2.5$ nm are shown in Fig. 1. The large area view shows well-defined NWs with uniform width and spacing while the insets display a magnified image of the NW arrays.

The L-shaped NWs were fabricated by using the tilted shadow deposition technique [21], which overcomes the various limitations of the multilevel electron-beam lithographic approach described including the issue of alignment of the two contrasting ferromagnetic materials and formation of oxide layers at the material walls. The key advantage of this nanofabrication process is that the successive deposition steps are self-aligned. It makes it possible to decrease the width of the formed elements with respect to the width of the used photoresist lithographic pattern. To create the L-shaped NWs, the NWs have a step modulation along their width with different width coverage thus making the top NWs positioned asymmetrically with respect to the photoresist pattern. This is

the result of tilting the sample with respect to the direction of the flux of the evaporated material which breaks the symmetry of the electron-beam evaporation configuration.

Magnetization vs magnetic-field loops were measured by using a Quantum Design MPMS superconducting quantum interference device (SQUID) magnetometer and magneto-optical Kerr effect (MOKE) using a photoelastic modulator operating at 50 kHz and lock-in amplification. Hysteresis loops were measured in the longitudinal configuration by sweeping the applied magnetic field between +0.8 and −0.8 kOe along the length of the NWs (easy magnetization direction). All the loops were taken at room temperature. The use of two magnetometry techniques is important because MOKE has essentially a surface sensitivity with a penetration depth of about 15–20 nm while SQUID is a bulk method providing information on the magnetic behavior of the entire NW volume.

BLS spectra of the thermally excited SWs were measured at room temperature in the backscattering geometry by using a (3+3)-pass tandem Fabry-Perot interferometer. Cross polarization between the incident and the scattered beams was employed in order to minimize the phonon contribution to the spectra. By varying the laser light incidence angle θ, the dispersion of SWs and consequently the magnonic band structure for the investigated NW arrays are mapped across several Brillouin zones, i.e., over the range of the magnon in-plane wave vector $k = (4\pi/\lambda) \times \sin(\theta)$ [33]. In our setup, we use a $\lambda = 532$-nm green light of a diode-pumped solid-state laser and the incident angle θ can be varied from 0° to 60°. This corresponds to a change in the in-plane wave-vector absolute value k in the range between 0 and 2.05×10^7rad/m. The measurements were performed in the Damon-Eshbach configuration, i.e., with the SW wave vector (k) swept along the periodicity direction of the arrays and perpendicular to the magnetic-field H applied parallel to the NWs length.

III. THEORY

In order to calculate the periodic dispersion of SWs, we employ a numerical code based on the solution of the linearized Landau-Lifshitz (LL) equation in the magnetostatic approximation [12,34]. We use a description of the dynamic dipole field of the precessing magnetization in the form of a 2D Green's function that accounts for both the self-demagnetizing (dipolar) field of each individual NW and the collective demagnetizing field of the dense array of wires [11]. We also include the contribution from the effective exchange field of dynamic magnetization to the magnetization dynamics.

The integral operator involving the Green function and the differential operator of the effective exchange field are discretized on a square mesh, which fills the stripe cross section. The discretization of the operators transforms the LL equation into an eigenvalue/eigenvector problem for a matrix. The eigenvalues of the matrix represent eigenfrequencies of the Bloch SW modes for the periodic NW array for a given Bloch wave number. The eigenvectors are the spatial profiles for the respective modes. The eigenvectors are complex valued; thus, they contain information about the phase of magnetization oscillation at any particular point on the NW cross section.

The discretization of the exchange operator requires exchange boundary conditions at the magnetic surfaces of the stack—the upper surface of the upper layer, the interface of the lower layer with the substrate, the part of the upper surface of the lower layer that it is not covered by Cu, and the lateral surfaces of both magnetic layers. We assume the "unpinned surface spins" boundary conditions at all those interfaces, but also include an effective perpendicular anisotropy field acting only for the surface cells of the discrete mesh. (The effective field is directed perpendicular to the respective surface—along the normal to the array plane for the upper and lower surfaces and in the array plane for the lateral surfaces.) Numerically, the introduction of the field of the "surface" anisotropy is equivalent to partial pinning of the surface spins. The surface anisotropy field is introduced as an adjustable parameter that allows us to improve the quality of fits of the experimental data with our theory. As a result, the strength of the surface anisotropy is individual for each individual sample. Magnetic parameters used in the calculations are $4\pi M_s(\mathrm{Py}) = 11$ kOe and $4\pi M_s(\mathrm{Fe}) = 22$ kOe for the saturation magnetization, exchange stiffness constant $A(\mathrm{Py}) = 1 \times 10^{-6}$erg cm^{-1} and $A(\mathrm{Fe}) = 2 \times 10^{-6}$erg cm^{-1}, $\gamma(Py) = 2.90$ MHz/Oe and $\gamma(\mathrm{Fe}) = 3.05$ MHz/Oe . These values are extracted from measurements of the frequency dispersion of SWs in continuous (unpatterned) reference Fe/Cu(t)/Py films.

We solve the constructed eigenvalue/eigenvector problem numerically using the numerical tools built into MATHCAD. The matrix elements are calculated for a given value of the Bloch vector; then, the matrix's eigenvalues are found numerically. Repeating this procedure for a range of Bloch wave vectors produces a graph of the SW dispersion. Calculating eigenvectors of the matrix in the same program run allows us to visualize the respective amplitude and phase of the mode profiles in the two ferromagnetic layers. In all cases, the profiles are calculated for $k = 0$ and are averaged over the thicknesses of both the Fe and the Py layers.

At this stage, it is useful to introduce the mechanism for the creation of collective Bloch SWs waves on an array of dipole-coupled magnetic elements. The collective dynamics arises because the elements (wires in the present case) are coupled by the dynamic stray field created by the precessing magnetization. If an object is magnetized uniformly, the stray field it produced in its vicinity is the largest and the most far-reaching. Conversely, if the magnetization vector for a part of the object points in the opposite direction with respect to the remainder of the object's volume, the net magnetic moment (NMM) decreases. This produces a smaller stray field. The field is also more localized at the object (does not extend that far as in the case of the uniform magnetization).

As a result, the mode characterized by the maximum NMM inside the NW is expected to demonstrate the most pronounced collective character. In the present case, this depends on both the spatial profiles of the modes within each layer and on the relative phase of precession (in-phase or out-of-phase) of the magnetization vectors within the two NW layers (see Figs. 5 and 8). The mode with the largest dynamic NMM will be seen as the broadest frequency band for the mode. The bandwidth is maximized, because the larger the NMM for the mode, the farther the dipole field extends spatially.

For the center of the Brillouin zone ($k = 0$), the magnetic moments of the nearest-neighbor NWs precess in-phase. This implies that at any moment of time, they point in the same direction. This allows the field lines of the in-plane component of the dynamic stray field of every individual wire to terminate at the magnetic moments of the nearest neighbors instead of extending to infinity. This decreases the density of the collective dipole energy for the array with respect to the case of the respective single wire. Accordingly, the eigenfrequency of the collective mode is smaller than for the respective mode of an individual wire.

In the opposite case of the edge of the first Brillouin zone ($k = \pi/a$), the in-plane magnetic moments of the nearest-neighbor wires are pointing in the opposite directions. The field lines of the dynamic stray field cannot then terminate at the magnetic moments of the nearest neighbors. They have to wind back into the wire itself, where they need to run across the whole in-plane size of the wire until they are able to turn by 180° one more time and terminate at the magnetic moments of the opposite edge of the wire. As a result, a strong dynamic demagnetizing field is present inside each wire, whose field lines are antialigned to the local magnetization vector. The antialignment yields a larger dipole energy density with respect to a single wire and thus an increase in frequency with respect to the single-wire case.

Thus, the dipole coupling of wires produces a variation in frequency across the Brillouin zone. Put differently, it makes the mode dispersive. Obviously, the smaller the NMM, the more localized the stray field, the smaller dipole coupling of wires, and the narrower the mode frequency band. For the interwire distances that can be reliably created with the optical deep-ultraviolet lithography, only the stray field of the mode with the largest magnetic moment is usually strong enough not to die off completely before reaching the nearest-neighbor wires, thus making this mode the only dispersive mode of the spectrum.

IV. RESULTS AND DISCUSSION

A. MOKE and SQUID loops

Shown in Fig. 2 are the representative MOKE (black points), and SQUID (red points), *M-H* loops measured for NW arrays as a function of Cu layer thickness (t) for magnetic fields applied parallel to the NW length. The evolution of the magnetization reversal process as a function of the Cu spacer layer thickness can be attributed to the different coupling mechanisms between the two magnetic layers.

As expected, the MOKE loops for the L-shaped NW arrays for $t = 0$ and 2.5 nm are of square shapes due to the ferromagnetic-type interlayer exchange interaction between the Py and Fe NWs. They are characterized by coercivities of 150 and 240 Oe, respectively. This difference is an indication of the strength of the exchange coupling. For $t = 0$ the two layers are strongly exchange coupled due to the direct contact between the Fe and Py layers, thus resulting in a smaller coercivity and switching field distribution when compared with similar structures with $t = 2.5$nm. The SQUID loops show similar behavior in terms of coercivity; however, the whole loop shape is more complex. In particular, after the reversal, small steps appear, followed by a gradual and less and less sharp evolution toward saturation with respect to the MOKE curve. This can be interpreted as due to the presence of the strong ferromagnetic exchange coupling between the two Fe and Py layers. The switching of the soft and wider Py NWs exerts an additional field on the top Fe layer. This field, coupled with the externally applied field, causes the magnetic moment of the Fe NWs to rotate prior to switching, leading to a gradual decrease in magnetization as observed in Fig. 2.

For $t = 5$ and 10 nm, Py and Fe NWs are exchange decoupled and magnetostatic interaction starts to play a significant role in the reversal mechanism, as discussed in previous work [35]. On reversing the applied field from the positive saturation, a sudden drop in magnetization, proportional to the Py magnetization fraction within each NW (about 40%), occurs. This is in good agreement with the experimental result. This drop is more pronounced in the SQUID loop (about 50%) and it is associated with the magnetization reversal of the (softer) Py NW layer at about 115 Oe followed by the reversal of the Fe one at 375 and 500 Oe for the $t = 5$ and 10 nm, respectively. In between, a plateau where the Py and Fe magnetization vectors point in opposite directions is observed, thus forming the AP ground state whose field range for $t = 10$ nm (385 Oe) is much wider than for $t = 5$ nm (260) Oe. The presence of this plateau, where magnetization vectors point in opposite direction, has already been found for planar NW arrays consisting of two families of adjacent NWs having different width or materials [36,37].

As a general comment, we notice that the SQUID magnetization curves are less sharp than the MOKE ones and magnetization reversal occurs over a wider field range. The observed discrepancy is likely due to the different area probed and layer sensitivity by the two techniques. Indeed, the SQUID magnetometer records the total magnetic moment produced by the whole sample with the area of $4 \times 4\,\mathrm{mm}^2$, while the MOKE signal originates from a laser spot of about 50 microns in diameter and magnetic signal comes from the finite penetration depth of light (10–20 nm). One may expect a larger distribution of switching fields for individual NW over the much larger area of the sample than over the small laser spot.

For the rectangular cross-section Fe/Cu(t)/Py NWs (Fig. 2), MOKE and SQUID loops are very similar for $t = 0$ and 2.5 nm. Both are square and are characterized by a similar coercivity of about 260 Oe. This indicates that the Fe and Py NW layers are coupled by interlayer exchange interaction as previously discussed for the L-shaped NWs with the same t values. For $t = 5$ and 10 nm, the SQUID loop features a distinct two-step switching corresponding to the separate magnetization reversals of the Py and Fe NWs while the MOKE loop is almost square. We attribute this behavior to the fact that Fe and Py layers are exchange decoupled and the reverse independently. The difference in the loop shapes observed by the different techniques is attributed to the finite penetration depth of laser light (15–20 nm) which, due to the uniform coverage of the layers, does not probe the bottom Py layer. Hence, the reversal of the bottom layer is not visible. As expected from the SQUID loop, the field region for the AP alignment is smaller (about 70 Oe) when compared with that for the L-shaped NWs, where the Fe layer width is much

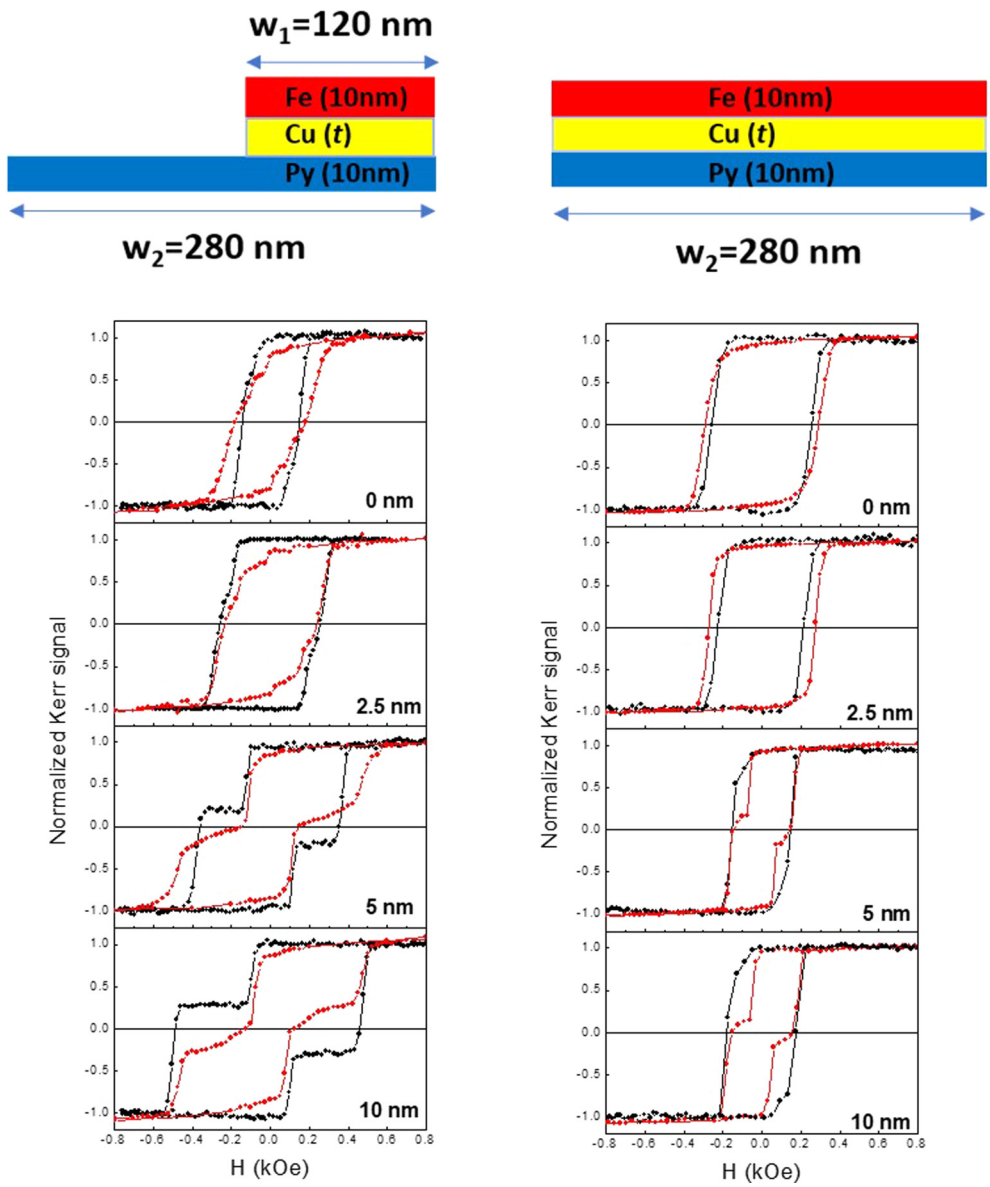

FIG. 2. Measured MOKE (black points) and SQUID (red points) loops measured for NWs with different thicknesses (t) of the Cu layer. A magnetic field is applied parallel to the NWs length.

smaller than the Py width. This supports the idea that the field range for the AP alignment of the magnetization vectors for the two magnetic layers can be effectively controlled by changing the width of the NW layers.

B. Fe/Cu(t)/Py L-shaped NW arrays: Spin-wave band structure and mode spatial profiles

Figure 3 shows the BLS spectra measured at $k = 0$ (light at normal incidence upon the sample surface, $\theta = 0°$) for all the investigated L-shaped NWs in the P and AP states for different t values. Spectra have a very good signal-to-noise ratio and are characterized by the presence of several well-resolved peaks whose frequency range depends on the magnetization configuration. In more detail, the spectrum for $t = 0$ nm in the P state contains a single peak at about 6.3 GHz, while for $t = 2.5$ nm the spectrum is completely different both in terms of the number of peaks and their frequency position. Furthermore, the lowest-frequency peak shifts down to 4.9 GHz and three other peaks become visible in the range between 7.1 and 9.5 GHz. On further increasing t to 5 nm and finally to 10 nm, the whole spectra undergo frequency upshifts and the lowest-frequency peaks move from about 5.8 to 7.0 GHz. At higher frequencies, other peaks also appear. For $t = 2.5$ and 5.0 nm the two lowest-frequency peaks have comparable intensities while for $t = 10$ nm the lowest-frequency peak has the largest intensity.

The AP configuration can be stabilized only for $t = 5$ and 10 nm at $H = +200$ Oe. Therefore in Fig. 3 we show spectra for these two NW arrays, only. It is worth noticing that in this case, the overall spectrum is downshifted in frequency with respect to the ones measured in P state and it is the second-lowest frequency peak which exhibits the largest intensity. We would like to note that in the spectra shown in Fig. 3

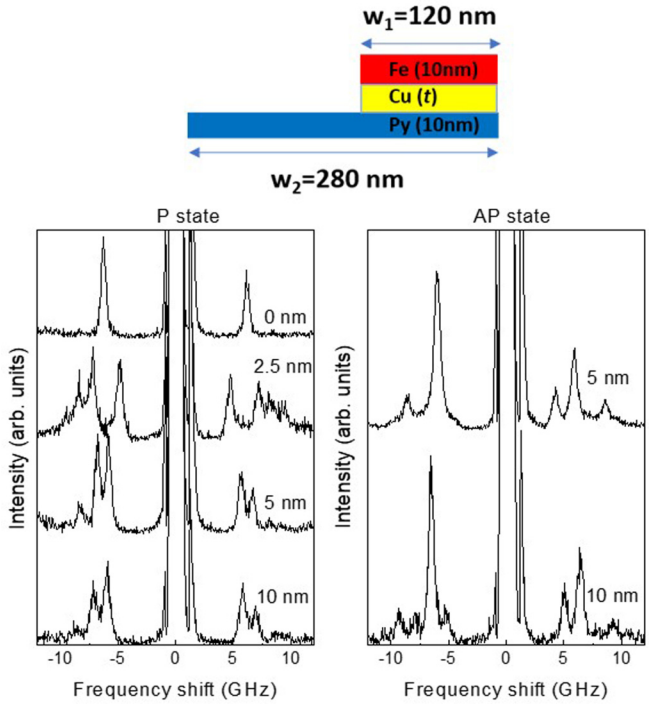

FIG. 3. Measured BLS spectra at $k = 0$ for different Cu thicknesses for L-shaped NWs in the P and AP magnetization configurations. All the spectra were taken for $H = +200$ Oe.

($k = 0$), higher-order modes are not visible. They become experimentally detectable on increasing k values due to the k-vector dependence of the BLS cross section.

In Fig. 4, we show the SW dispersion relation by plotting the dependence of the frequencies of detected modes as a function of the wave number k in the direction of the array periodicity. We see a very good overall agreement between the theory and the experiment for all the frequency modes. The periodicity of the frequency oscillation (π/a, the width of the Brillouin zone) is independent of the thickness of the layers since all the investigated NW arrays have the same lattice periodicity. When the two Fe and Py layers are in direct contact ($t = 0$) or separated by Cu spacer of thickness $t = 2.5$ nm, the lowest-frequency mode shows a periodic frequency dispersion induced by the artificial periodicity of the NWs while modes at higher frequencies exhibit flat dispersion. We remark that for $t = 2.5$ nm, the frequency separation between successive modes is larger than that for $t = 0$ nm.

For $t = 5$ and 10 nm, we are able to follow the evolution of five modes in the entire k-vector range investigated. For $t = 5$ nm, it is the second-lowest frequency mode which now exhibits a sizable width of the magnonic band, while for $t =$ 10 nm, it is again the lowest-frequency mode which exhibits a dispersive behavior.

In the AP magnetization configuration observed for $t =$ 5 and 10 nm, five distinct modes are observed and their frequency evolution over the entire k-vector range has been followed. A significant frequency downshift for all the modes and a reduction of the magnonic bandwidth for the dispersive mode (second-lowest frequency mode) is observed with respect to the P case. All other modes are dispersionless, i.e., their frequencies do not change over the whole range of wave vectors investigated.

We would like to mention that for $t = 5$ and 10 nm, band-structure calculations have been carried out assuming that the two magnetic layers are exchange decoupled, as inferred from the measured hysteresis loops, and their mutual interaction occurs via the dynamic dipolar interlayer coupling. This provides a satisfactory agreement between calculations and experimental data.

As a general comment, we attribute the small bandwidth measured for all the NW arrays to the relatively large distance between adjacent NWs ($s = 280$ nm) so that the dynamic dipolar field created by an individual NW dies off almost completely before reaching the nearest-neighbor NWs. In addition, the reduction in the interwire dipole coupling observed for the AP state with respect to the P state is attributed to the effect of the opposite senses of precession for the two layers. At any moment of time, the horizontal component of the dynamic magnetization is in-phase for both layers but the vertical one is in antiphase for the layers. The antiphase component does not produce a stray field at larger distances. Therefore, the interwire coupling in AP state is due to only one (in-phase) dynamic magnetization component where both components oscillate in-phase in both layers.

As follows from the general description of the formation of the collective Bloch SWs on the array from the last part of the Theory section in order to gain a detailed understanding of the individual mode character (i.e., stationary or dispersive), it is instructive to look at their spatial profiles of the modes across the NW width and consider the phase difference between the magnetization oscillations in the Py and Fe layers within each NW [20]. As a general rule for single-layer NW, modes with an odd number of nodes across the NW width are characterized by a zero-dynamic NMM and therefore they do not create a dynamic dipolar (stray) field outside the nanowire itself. For this reason, these resonances are not efficiently coupled through the array and exhibit a stationary character with almost flat dispersion. Contrarily, modes with an even number are characterized by a dispersive behavior. This is particularly true for the lowest-frequency mode with a quasiuniform profile of the dynamic magnetization. For layered NWs, like the ones investigated in the present paper, one has also to consider the phase relation between the dynamic magnetization in the two layers. If the magnetization vectors for the layers precess in antiphase ("antiphase modes" or APM), NMM for nanowires is small. (It is not exactly zero because the layers are made of different materials.) Conversely, in the magnetization vectors precess in phase ("in-phase modes" or IPM), NMM for the wires is much larger in the general case. APMs are usually dispersionless and nonpropagating (or stationary), while IPMs usually exhibit a large amplitude of the magnonic band and therefore are dispersive and propagating, especially the fundamental IPM (FIPM). From the experimental point of view, by varying k in the BLS measurements, we are probing the width of the magnonic band and thus we can understand which modes are propagating and which ones are stationary.

These are shown in Fig. 5 for $k = 0$ for all the Cu spacer values and for both the P and AP states. Each L-shaped NW may be represented as two effective NWs having different widths and thicknesses. The area $0 < x < 160$ nm is a

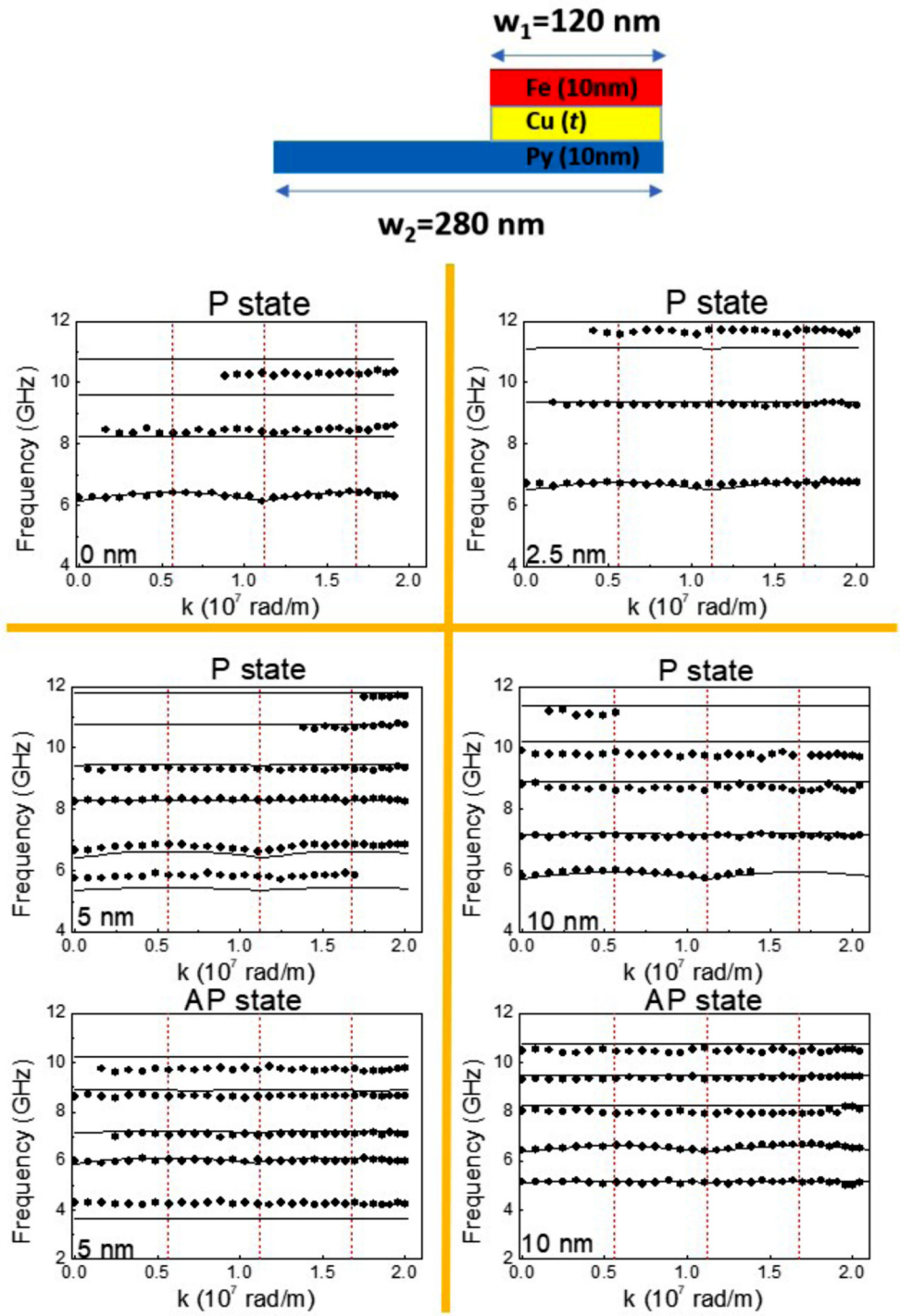

FIG. 4. Measured (points) and calculated (lines) magnonic band structure for the Fe/Cu(t)/Py L-shaped NW arrays in the P and AP states. In both cases, a magnetic field $H = +200$ Oe is applied along the NW length. Red dashed lines indicate the edges of the BZs ($n\pi/a$, where $n = 1,2,3\ldots$).

10-nm-thick single-layer Py NW and we refer to this region as the THIN portion of the L-shaped NW while the area $160 < x < 280$ nm corresponds to a 10-nm-thick Py layer overlaid with a Fe/Cu(t) NW layer. We will refer to it as the THICK portion of the NW. These two effective NWs are in a lateral exchange contact through a "virtual interface" $x = 120$ nm, running across the Py layer of the actual L-shaped NW. They are also coupled by their dipole fields.

Let us start by describing the results for the P case. When $t = 0$ and 2.5 nm, one sees that the amplitude of the dynamic magnetization is mainly localized inside the THIN NW portion. The profiles are characterized by an increasing number of nodes within the THIN portion, while their amplitude is almost zero in the THICK region. In this region, the magnetization precession is in-phase for the two magnetic layers for all the modes. One also sees that only

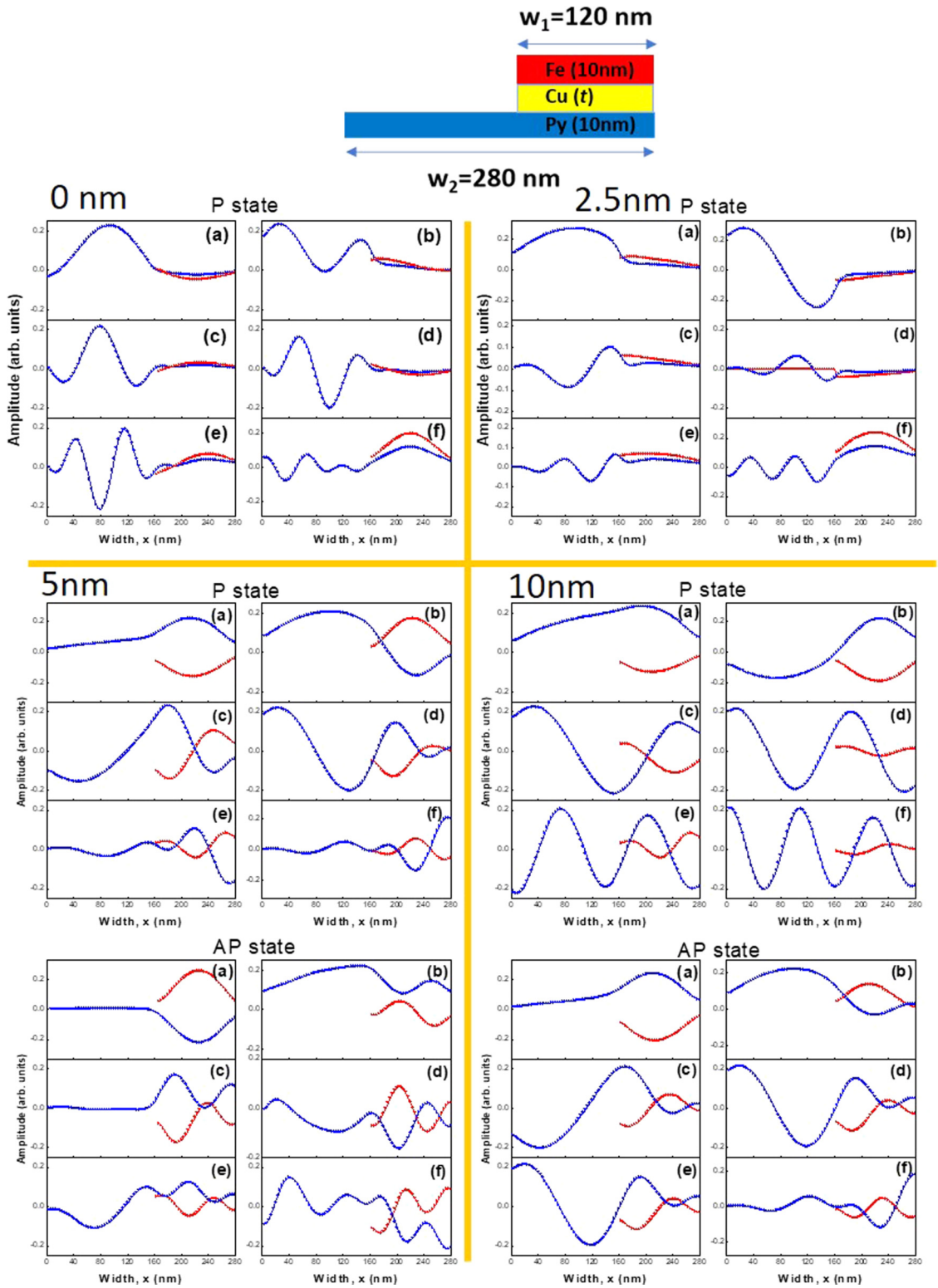

FIG. 5. Calculated amplitude of the out-of-plane component of the dynamic magnetization for the six-lowest frequency modes as a function of the coordinate along the width of L-shaped NWs. The profiles are calculated for the center of the BZ ($k = 0$) and for both P and AP states. The applied field is $H = +200$ Oe for all the Cu thicknesses. The Cu spacer thickness varies from 0 (top-left panel set) to 10 nm (bottom-right panel set). The red and blue curves refer to the spatial profile within either the Fe or the Py layers, respectively.

the lowest-frequency mode, characterized by a quasiuniform profile within the THIN region, displays a sizable magnonic bandwidth. This mode is also the mode that exhibits the largest BLS intensity in the spectrum shown in Fig. 3. All other modes have standing-wave-like behavior with flat dispersion. The sixth-lowest frequency mode (panel f of Fig. 5) is an exception—the magnetization amplitude for that mode is significantly different from zero for both the magnetic layers

of the THICK NW portion. This mode is supposed to exhibit a dispersive character; however, this behavior is not detected in the experiment because of the rather large frequency for the mode. This behavior is not different from the typical behavior of single-layer NWs, where only the lowest-frequency mode exhibits a sizable dispersion over the entire wave-vector range [38]. For the two remaining arrays having $t = 5$ and 10 nm, we notice that the dynamic magnetization vectors for the Py and Fe oscillate in antiphase for all the modes. This is ascribed to the presence of the Cu nonmagnetic spacer which exchange decouples the magnetization dynamics in the two ferromagnetic layers [39].

More in detail, for $t = 5$ nm, the lowest-frequency mode (panel a) has a zero-dynamic NMM across the NW and therefore it has an almost flat dispersion over the entire wave-vector range investigated. The second- and third-lowest frequency modes (panels b and c, respectively) have similar profiles over the entire NW width but that of panel b has larger dynamic magnetization amplitude in the THIN NW portion ($120 < x < 280$ nm). Therefore, this mode is the one characterized by the largest magnonic bandwidth. The modes at yet higher frequencies (panels d–f) are characterized by an increasing number of nodes in the THICK part and with a negligible dynamic NMM across the two layers. Therefore, they are essentially nondispersive. A different situation occurs for $t = 10$ nm where the lowest-frequency mode now has a nonzero-dynamic NMM. This is in agreement with a dispersive character for this mode, as seen from Fig. 4. All the other modes are characterized by a large number of nodes of the standing wave over the area of the NW cross section and have negligible-dynamic NMM. This results in the dispersionless character for the modes.

In the *AP* state, BLS measurements of SW dispersion and calculation of modes profiles have only been done for $t = 5$ and 10 nm. We notice that for both the Cu thicknesses the dynamic NMM within each NW is negligible with exception of the second-lowest frequency mode, which in turn is the only one that exhibits a sizable bandwidth. Therefore, all other modes are characterized by a flat frequency dispersion.

C. Fe/Cu(*t*)/Py rectangular NW arrays: Spin-wave band structure and mode spatial profiles

We now present experimental results and calculation for the Fe/Cu(t)/Py NWs with rectangular cross section in the *P* and *AP* state and compare them with those for the L-shaped NWs discussed above (Fig. 6).

In the P state for $t = 0$, three peaks are visible in the spectrum at $k = 0$ contrarily to what is observed for the L-shaped NW with the same Cu value. In addition, the peaks are within a higher frequency range (from 10 to 19 GHz) rather than below 11 GHz. On increasing the Cu thickness, the overall spectrum undergoes a frequency downshift, with the lowest-frequency peak sitting at about 5 GHz, while the largest-intensity peak moves upwards in frequency for $t =$ 5 nm and then remains constant in frequency. Regarding the spectra measured at $H = +100$ Oe in the *AP* state for $t = 5$ and 10 nm, the peaks are always below 10 GHz, with the minimum frequency of about 2 GHz. Differently from the case of the L-shaped NW, in the present case, we may expect that

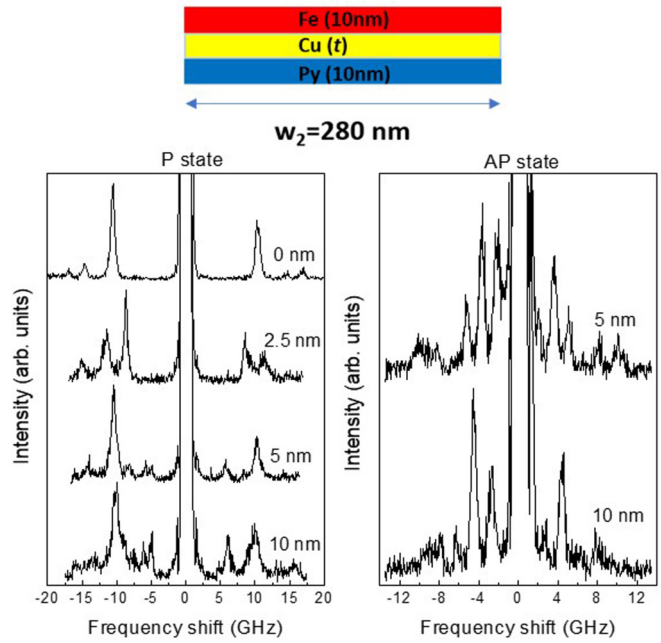

FIG. 6. Measured BLS spectra at $k = 0$ for different Cu thicknesses for rectangular NWs in the *P* and *AP* magnetization configurations. The spectra for the *AP* state of the rectangular NWs for $t = 5$ and 10 nm were measured at $H = +100$ Oe. The remaining spectra were taken at $H = +200$ Oe.

the BLS intensity mainly originates from the top Fe layer. This is because the bottom layer is fully covered by the overlying layers now.

The comparison between the measured and calculated collective SW dispersion for all the rectangular NW arrays in both the *P* and AP states is presented in Fig. 7. In all the cases, the experimental data are well reproduced by theoretical calculations, performed by using the magnetic parameters reported above. For $t = 0$ we observed the usual behavior where the dispersive low-frequency mode exhibits a sizable bandwidth (0.5 GHz) while all the other modes have higher frequencies and are almost dispersionless. Here the interlayer exchange interaction is taken into account. For the other Cu thicknesses, the SW dispersions are significantly different from the case of $t = 0$ nm. Interestingly, the dispersive mode is not at the bottom of the spectrum and the frequencies of the lowest-frequency modes are independent from k (flat dispersion). The dispersive modes are located in the frequency range between 10 and 12 GHz. The mode bandwidth is about 0.4 GHz for $t = 2.5$ nm and increases to 0.6 for both $t = 5$ and 10 nm.

Importantly, as mentioned above, the squareness of the hysteresis loop for $t = 2.5$ nm suggests the presence of interlayer exchange coupling for this structure. However, the presence of three nondispersive modes below the dispersive one in the spectrum of the collective Bloch SWs suggests that the dynamic dipole coupling of the Py layer to the Fe one dominates over the exchange layer coupling. Furthermore, the intensity for the lowest-frequency nondispersive mode is the largest in the measured BLS intensity spectrum for the sample (not shown). Indeed, the only explanation for the

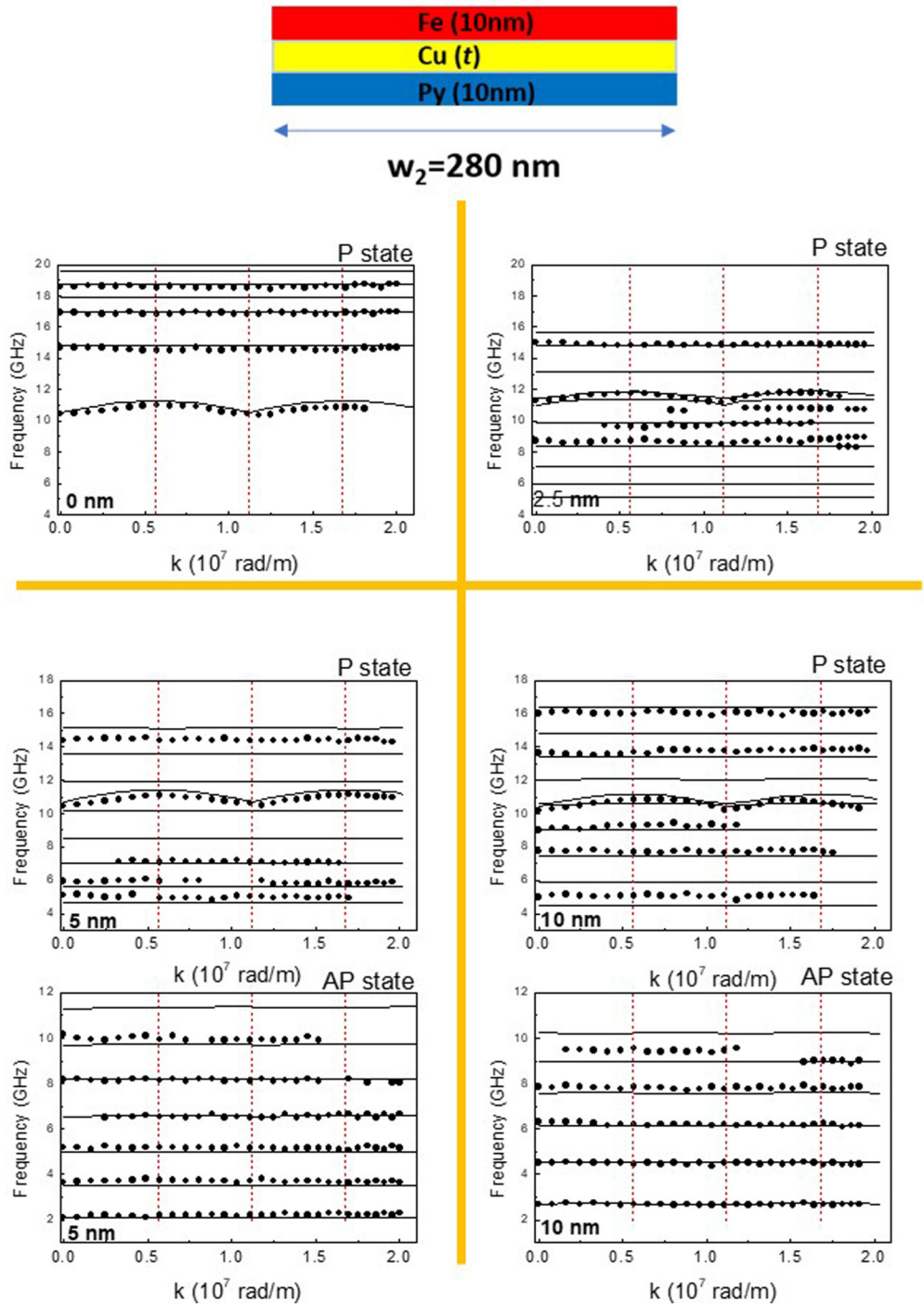

FIG. 7. Measured (points) and calculated (lines) magnonic band structure for the Fe/Cu(t)/Py rectangular cross-section NW arrays in the P and AP states and at $k = 0$. A magnetic field $H = +200$ Oe ($H = +100$ Oe) is applied along the NW length for the P (AP) configuration. Red dashed lines indicate the edges of the BZs ($n\pi/a$, where $n = 1,2,3\ldots$).

presence of the low-lying nondispersive modes characterized by high BLS intensity is that these modes are modes of optic type (out-of-phase precession). To confirm this fact, we carried out dispersion calculations for a range of the interlayer exchange constants A_{12}.

We started with a particular A_{12} value that we denote as $A_{12}^{(\mathrm{Fe})}$ that is equal to the intralayer exchange constant for Fe divided by the unit-cell size for it [$A_{12}^{(\mathrm{Fe})} = (2 \times 10^{-6}\mathrm{erg/cm})/(0.286 \times 10^{-6}\mathrm{cm})$] and gradually decreased it. As expected, we found that for A_{12} values comparable to $A_{12}^{(\mathrm{Fe})}$ the dispersive mode is the lowest in the simulated spectrum, and all modes in the spectrum are of acoustic types [40]. This provides evidence of a strong contribution of the interlayer exchange to the spectrum form. For a much lower interlayer exchange stiffness value $A_{12} = 0.002A_{12}^{(\mathrm{Fe})}$, nondispersive modes of optic type appeared below the dispersive acoustic (in-phase

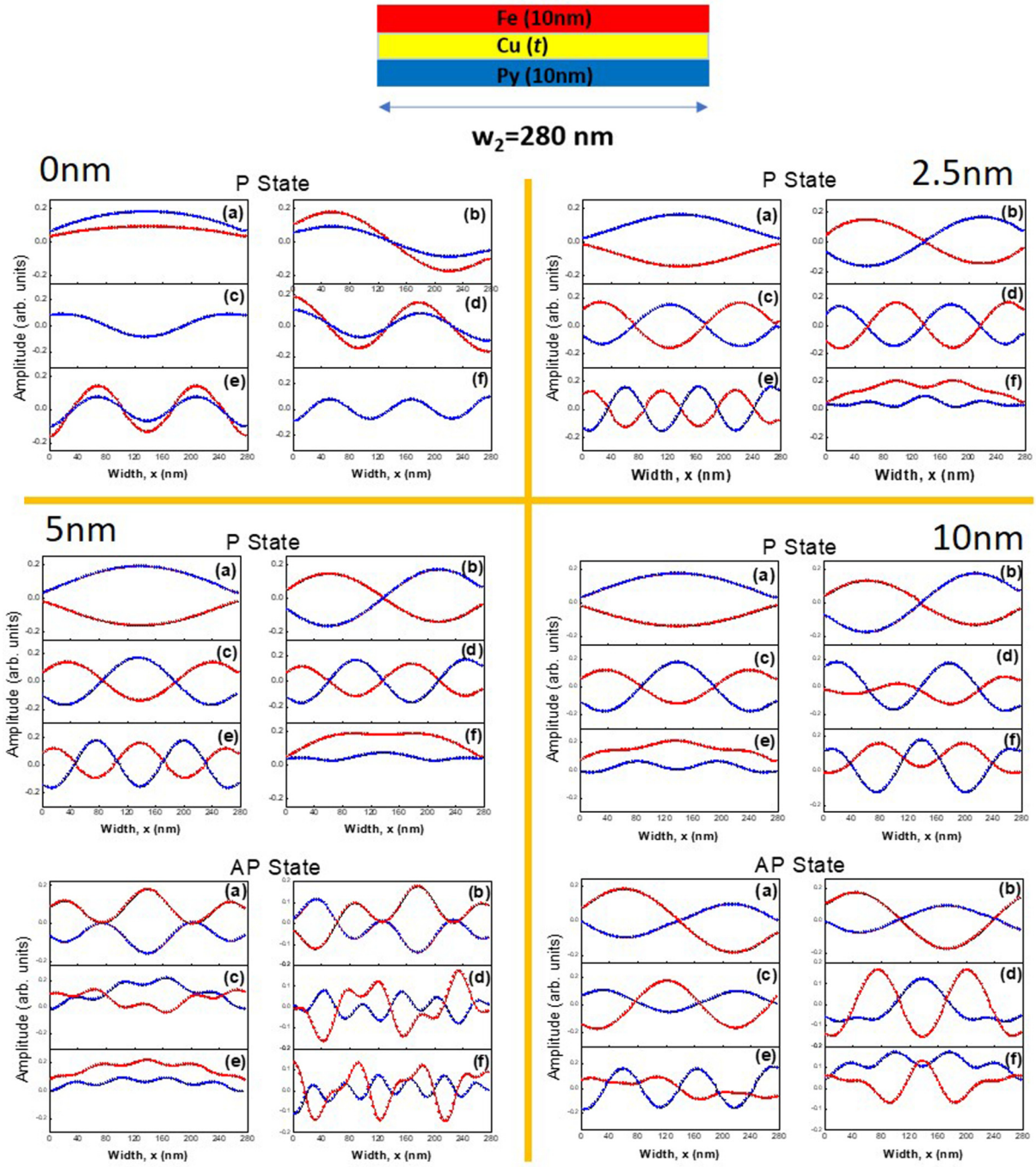

FIG. 8. Calculated amplitude of the out-of-plane component of the dynamic magnetization for the six-lowest frequency modes as a function of the coordinate along the width of rectangular shaped NWs. The Cu spacer thickness varies from 0 (top-left panel set) to 10 nm (bottom-right panel set). The profiles are calculated for the center of the BZ ($k = 0$) and for both P and AP states. The applied field is $H = +200$ Oe ($+100$ Oe) for the Cu thickness of 0 and 2.5 (5 and 10 nm). Red (blue) traces refers to the Fe and Py magnetic layers, respectively.

precession) one. This suggests that $A_{12} = 0.002A_{12}^{(\mathrm{Fe})}$ is the threshold below which dipole coupling between the two ferromagnetic layers starts to dominate over the exchange one.

This qualitative difference between the slow dynamics (hysteresis loop) and the microwave dynamics can be explained by the perfectly linear character of the SW dynamics and the strongly nonlinear character of the effect of magnetization switching. This fundamental difference in the process character obviously leads to a difference in the "threshold" A_{12} values for the onset of the antiferromagnetic static magnetization configuration and the appearance of the optic modes in the SW spectrum.

In the AP state ($t = 5$ and 10 nm), the dispersions are flat over the entire k-value range under investigation for every observed mode. The total band structure is downshifted and

modes have larger frequency separation than those observed in the P state. Even in these cases, we assumed the layers to be coupled by interlayer dynamic coupling.

All these features are easily explained by inspection of the calculated mode profiles shown in Fig. 8. For $t = 0$ nm, magnetization precession is in-phase in the two layers and the low-frequency quasifundamental mode has no nodes within the NW cross section. Consequently, it has a nonzero-dynamic NMM. The dynamic stray field of the precessing magnetic moment ensures efficient coupling of nearest-neighbor NWS on the array. This leads to a sizable frequency dispersion of this mode.

For $t \geqslant 2.5$ nm in the P state, the precession of the layers' magnetization vectors is always out-of-phase with the only difference being the frequency position of the quasifundamental mode which has the most pronounced dispersive character. Both for $t = 2.5$ and 5 nm, it is the sixth-lowest frequency mode from the bottom of the spectrum while it is the sixth lowest for $t = 10$ nm. The profiles in the AP configuration indicate that all the modes have zero-dynamic NMM when averaged over both the magnetic layers, with exception of the fifth mode from the bottom for $t = 5$ nm. We notice that in this configuration the profiles deviate from the sinusoidal shape and are less symmetric with respect to the middle of the NW width. This is because the amplitude of the dynamic magnetization is a complex-valued quantity in this case, and we plot its real-valued parts. The moduli of these complex-valued profiles are symmetric [41]. However, the information on the precession phase is lost for those profiles. Therefore, we choose to show the real parts of the profiles.

We would like also to remark that the magnonic bandwidth measured for the rectangular NWs are always larger than those measured for the L-shaped NW arrays. This is attributed to the fact that for the L-shaped cross-section NWs, the pronounced mode localization on the THIN region makes the effective distance between nearest-neighbor NWs larger than the real one. This reduces the dynamic dipolar field which couples the nearest neighbors.

V. CONCLUSIONS

We have studied experimentally and theoretically the frequency dispersion of collective spin waves in dense arrays of Fe/Cu(t)/Py nanowires with either symmetric or asymmetric cross section. For asymmetric (L-shaped) cross-section nanowires we have found that when $t \leqslant 2.5$ nm, the two layers reverse simultaneously due to strong interlayer exchange coupling across the interface. Only acoustic modes are detected for this thickness of the Cu spacer, only. For larger values of the Cu spacer thickness, the reversal of the static magnetization vectors for the two layers is mainly mediated by magnetostatic interactions. Due to the different switching fields of the layer, a region of antiparallel alignment between the two layers magnetization is observed. In this case, modes with both in-phase and out-of-phase precession of dynamic magnetizations observed.

For symmetric (rectangular) cross-section nanowires, we have found that the range of magnetic fields, where the two magnetization vectors are aligned antiparallel, is lower than in the case of asymmetric nanowires. The character of the observed spin-wave band structure indicates that for $t \geqslant 2.5$ nm the dominating contribution to the spin-wave dynamics originates from the dynamic dipolar interaction, and only for $t = 0$ the interlayer exchange interaction plays a significant role in the formation of the spin-wave spectrum. As a consequence, whereas the lowest-frequency mode for $t = 0$ exhibits a sizable magnonic bandwidth when $t \geqslant 2.5$ nm the lowest-frequency mode is dispersionless. The results presented in this work represent a step forward in understanding the magnonic band structure in layered magnonic crystals where the propagation of collective Bloch spin waves can be controlled by changing the relative orientation of the two magnetization vectors from parallel to antiparallel as well the thickness of the nonmagnetic Cu spacer. These findings may allow building reprogrammable magnonic networks and devices.

ACKNOWLEDGMENT

This work was supported by the Ministry of Education, Singapore Tier 2 funding via Grant No. R-263-000-C61-112.

[1] M. Krawczyk and D. Grundler, J. Phys.: Condens. Matter **26**, 123202 (2014).
[2] J. Topp, D. Heitmann, M. P. Kostylev, and D. Grundler, Phys. Rev. Lett. **104**, 207205 (2010).
[3] G. Gubbiotti, X. Zhou, Z. Haghshenasfard, M. G. Cottam, and A. O. Adeyeye, Phys. Rev. B **97**, 134428 (2018).
[4] M. Vogel, A. V. Chumak, E. H. Waller, T. Langner, V. I. Vasyuchka, B. Hillebrands, and G. von Freymann, Nat. Phys. **11**, 487 (2015).
[5] V. V. Kruglyak, S. O. Demokritov, and D. Grundler, J. Phys. D: Appl. Phys. **43**, 264001 (2010).
[6] A. V. Chumak, A. A. Serga, and B. Hillebrands, Nat. Commun. **5**, 4700 (2014).
[7] S. J. Hämäläinen, M. Madami, H. Qin, G. Gubbiotti, and S. van Dijken, Nat. Commun. **9**, 4853 (2018).
[8] M. Inoue, A. Baryshev, H. Takagi, P. B. Lim, K. Hatafuku, J. Noda, and K. Togo, Appl. Phys. Lett. **98**, 132511 (2011).
[9] A. A. Nikitin, A. B. Ustinov, A. A. Semenov, A. V. Chumak, A. A. Serga, V. I. Vasyuchka, E. Lähderanta, B. A. Kalinikos, and B. Hillebrands, Appl. Phys. Lett. **106**, 102405 (2015).
[10] Z. K. Wang, V. L. Zhang, H. S. Lim, S. C. Ng, M. H. Kuok, S. Jain, and A. O. Adeyeye, Appl. Phys. Lett. **94**, 083112 (2009).
[11] Z. K. Wang, V. L. Zhang, H. S. Lim, S. C. Ng, M. H. Kuok, S. Jain, and A. O. Adeyeye, ACS Nano **4**, 643 (2010).
[12] F. S. Ma, H. S. Lim, Z. K. Wang, S. N. Piramanayagam, S. C. Ng, and M. H. Kuok, Appl. Phys. Lett. **98**, 153107 (2011).
[13] G. Duerr, M. Madami, S. Neusser, S. Tacchi, G. Gubbiotti, G. Carlotti, and D. Grundler, Appl. Phys. Lett. **99**, 202502 (2011).
[14] F. S. Ma, H. S. Lim, Z. K. Wang, S. N. Piramanayagam, S. C. Ng, and M. H. Kuok, IEEE Trans. Magn. **47**, 2689 (2011).
[15] J. O. Vasseur, L. Dobrzynski, B. Djafari-Rouhani, and H. Puszkarski, Phys. Rev. B **54**, 1043 (1996)
[16] S. Tacchi, G. Duerr, J. W. Klos, M. Madami, S. Neusser, G. Gubbiotti, G. Carlotti, M. Krawczyk, and D. Grundler, Phys. Rev. Lett. **109**, 137202 (2012).

[17] G. Gubbiotti, S. Tacchi, M. Madami, G. Carlotti, S. Jain, A. O. Adeyeye, and M. P. Kostylev, App. Phys. Lett. **100**, 162407 (2012).
[18] S. Tacchi, G. Gubbiotti, M. Madami, and G. Carlotti, J. Phys.: Condens. Matter **29**, 073001 (2017).
[19] H. Puszkarski and M. Krawczyk, Solid State Phenom. **94**, 125 (2003).
[20] S. Mamica, M. Krawczyk, M. L. Sokolovskyy, and J. Romero-Vivas, Phys. Rev. B **86**, 144402 (2012).
[21] G. Gubbiotti, R. Silvani, S. Tacchi, M. Madami, G. Carlotti, Z. Yang, A. O. Adeyeye, and M. Kostylev, J. Phys. D: Appl. Phys. **50**, 105002 (2017).
[22] G. Gubbiotti, S. Tacchi, M. Madami, G. Carlotti, Z. Yang, J. Ding, A. O. Adeyeye, and M. Kostylev, Phys. Rev. B **93**, 184411 (2016).
[23] G. Gubbiotti, M. Kostylev, S. Tacchi, M. Madami, G. Carlotti, J. Ding, A. O. Adeyeye, F. Zighem, A. A. Stashkevich, E. Ivanov, and S. Samarin, J. Phys. D: Appl. Phys. **47**, 105003 (2014).
[24] G. Gubbiotti, X. Zhou, Z. Haghshenasfard, M. G. Cottam, A. O. Adeyeye, and M. Kostylev, Sci. Rep. **9**, 4617 (2019).
[25] P. Grünberg, J. Magn. Magn. Mater. **15-18**, 766 (1980).
[26] M. Madami, S. Tacchi, G. Carlotti, G. Gubbiotti, and R. L. Stamps, Phys. Rev. B **69**, 144408 (2004).
[27] B. Hillebrands, P. Baumgart, and G. Güntherodt, Appl. Phys. A **49**, 589 (1989).
[28] J. Jorzick, S. O. Demokritov, C. Mathieu, B. Hillebrands, B. Bartenlian, C. Chappert, F. Rousseaux, and A. N. Slavin, Phys. Rev. B **60**, 15194 (1999).
[29] S. O. Demokritov and B. Hillebrands, in *Spin Dynamics in Confined Magnetic Structures I*, edited by B. Hillebrands and K. Ounadjela (Springer, Berlin, 2003).
[30] M. Belmeguenai, M.S. Gabor, F. Zighem, D. Berling, Y. Roussigne, T. Petrisor, S.M. Cherif, C. Tiusan, O. Brinza, and P. Moch, J. Magn. Magn. Mater. **399**, 199 (2016).
[31] A. V. Sadovnikov, A. A. Grachev, S. A. Odintsov, A. A. Martyshkin, V. A. Gubanov, S. E. Sheshukova, and S. A. Nikitov, JETP Lett. **108**, 312 (2018).
[32] J. Ding and A. O. Adeyeye, Adv. Funct. Mater. **23**, 1684 (2013).
[33] M. Madami, G. Gubbiotti, S. Tacchi, and G. Carlotti, in *Solid State Physics*, edited by R. E. Camley and R. L. Stamps (Academic Press, Burlington, MA, 2012), Vol. 63, pp. 79–150.
[34] M. Kostylev, Z. Yang, I. S. Maksymov, J. Ding, S. Samarin, and A. O. Adeyeye, J. Appl. Phys. **119**, 103903 (2016).
[35] S. Goolaup, A. O. Adeyeye, and N. Singh, J. Appl. Phys. **100**, 114301 (2006).
[36] S. Goolaup, A. O. Adeyeye, N. Singh, and G. Gubbiotti, Phys. Rev. B **75**, 144430 (2007).
[37] V. L. Zhang, H. S. Lim, C. S. Lin, Z. K. Wang, S. C. Ng, M. H. Kuok, S. Jain, A. O. Adeyeye, and M. G. Cottam, Appl. Phys. Lett. **99**, 143118 (2011).
[38] G. Gubbiotti, S. Tacchi, G. Carlotti, N. Singh, S. Goolaup, A. O. Adeyeye, and M. Kostylev, Appl. Phys. Lett. **90**, 092503 (2007).
[39] P. A. Grünberg, Rev. Mod. Phys. **80**, 1531 (2008).
[40] Well below the threshold value of A, the frequency of the fundamental APM (FAPM) is significantly lower than for FIPM. In addition, the dynamic NMM for FAPM is significantly smaller than for FIPM. The frequencies of both modes grow with an increase in A_{12}. With approaching the threshold A_{12} value from below, FIPM and FAPM start to hybridize—the dynamic NMM for the FPAM (i.e., lower-frequency) mode starts to grow and the one for FIPM starts to fall. This happens through a significant reduction (almost to zero) of the amplitude of precession (and, thus, dynamic NMM) for the Fe layer in the FAPM case. At the same time, the dynamic NMM for the FIPM (i.e., higher-frequency) mode drops almost to zero through the reduction of the dynamic NMM for the Py layer. Near the threshold value, the dynamic NMM for the modes become equal, and shortly after, the signs of the dynamic NMM for the layers with the smaller NMM swap. The dynamic NMM for the Fe layer becomes of the same sign as for the Py layer for the lower-frequency mode, thus making that mode of the in-phase type. Conversely, for the higher-frequency mode, the dynamic-NMM sign for the Py layer becomes opposite to one for the Fe layer, thus making that mode of the antiphase type. With a further increase in A_{12}, the amplitudes of precession in the layers become comparable again for both types of modes. This makes the mode character well pronounced again, but now FAPM is characterized by a significantly higher frequency than FIPM.
[41] G. Gubbiotti, M. Kostylev, N. Sergeeva, M. Conti, G. Carlotti, T. Ono, A. N. Slavin, and A. Stashkevich, Phys. Rev. B **70**, 224422 (2004).